Lunar Navigation Beacon Network Using Global Navigation Satellite System Receivers

Evan J. Anzalone[a]*, Joel W. Getchius[b]. Jared O. Leggett[c]
Ben W. Ashman[d], Joel J. K. Parker[e], Luke B. Winternitz[f]

[a] *NASA/Marshall Space Flight Center, EV42, Huntsville, AL, 35801, USA,* evan.j.anzalone@nasa.gov
[b] *NASA/Goddard Space Flight Center/Omitron, Code 595, Greenbelt, MD 20771,USA,* joel.w.getchius@nasa.gov
[c] *NASA/Marshall Space Flight Center, EV42, Huntsville, AL, 35801,USA,* jared.o.legget@nasa.gov
[d] *NASA/Goddard Space Flight Center, Code 595, Greenbelt, MD 20771,USA,* benjamin.w.ashman@nasa.gov
[d] *NASA/Goddard Space Flight Center, Code 595, Greenbelt, MD 20771,USA,* joel.j.k.parker@nasa.gov
[e] *NASA/Goddard Space Flight Center, Code 596, Greenbelt, MD 20771,USA,* luke.b.winternitz@nasa.gov
* Corresponding Author

Abstract

With the increasing traffic in the lunar regime as part of NASA efforts to return humans to the moon. In order to support these missions, new capabilities are needed to support autonomous navigation and inter-asset communication. Additionally, with maturation and flight demonstration of increasingly capable small satellites, there is an opportunity to embed technology into a small spacecraft as part of companion missions. This paper addresses one such architecture, taking advantage of a lunar lander vehicle to host a companion spacecraft to build out lunar navigation and communication capability. The backbone of this spacecraft is the Navigator GPS receiver. This hardware has continually broken records on high altitude GPS coverage and has the potential to support autonomous navigation at lunar distances. This research proposes a large cubesat built around this technology and catching a ride to the moon via a lander mission. The concept of operations includes the spacecraft deploying prior to the lunar sphere of influence and manuevering to enter into a lunar orbit. With the Navigator receiver, this spacecraft is capable of a large amount of autonomy, with a limited need for ground-based orbit determination. This spacecraft will fly alongside the lander, acting as a navigation reference during cruise, descent, and post-landing for mission validation. To assess this mission scenario, three aspects are covered in detail herein: the feasibility and mission requirements for entering into a lunar orbit given deployment along a lander surface-bound trajectory, the performance capability of the receiver along this transfer trajectory and in lunar orbit, and the ability to support navigation of the lander itself. These three areas are discussed in detail, providing results that support feasibility of the mission and determination of initial requirements.
Keywords: Navigation, GNSS, Lunar Architecture, Beacon, Planetary Lander

Acronyms/Abbreviations
GNC – Guidance, Navigation, and Control
GNSS – Global Navigation Satellite System
GPS – Global Positioning Systems
IMU - Inertial Measurement Unit
LPL – Lunar Pallet Lander
MMS - Magnetospheric Multiscale Mission
SRM – Solid Rocket Motor
TCM – Trajectory Correction Manuever

1. Introduction

Recent priorities and investments, both government and commercial, are focusing on a return to the Lunar environment. In addition to an increase in science missions, a host of entities are developing human exploration missions. These investments lead towards a need for expanded architecture and functionality to support expansive and mature operations. In order to support numerous potential missions and maximize return, global coordination systems will be implemented to improve efficiency. To support and coordinate vehicles and explorers, a communication and navigation network will be needed to help guide missions and provide global coverage back to Earth.

This paper focuses on the design and architecture of a proposed GNC system that utilizes advances in small-form-factor technology with special enhancements in navigation sensor hardware to provide functionality for small satellite missions in the Lunar Regime. The key technology providing navigation relative to Earth is high altitude-capable Global Positioning System (GPS) or Global Navigation Satellite System (GNSS) receivers. The proposed system specifically relies on the NASA-developed Navigator GPS receiver, which has set high altitude records, achieving GPS-derived state updates at nearly half the distance to the moon. Recent studies indicate that this technology is capable of supporting strong navigation in the Lunar domain. In the proposed system, GPS will be used to provide a high accuracy navigation and timing reference to other spacecraft.

The proposed architecture takes advantage of the GPS-based state solutions to provide navigation capability with other spacecraft through communication-based navigation approaches, allowing for inter-

spacecraft (and ground rover) state estimation. The initial use case is to support a large payload lander on approach and descent to the Lunar surface. By embedding this hardware within a small spacecraft platform, this beacon will travel from Earth alongside the lander platform. Through the use of the Navigator receiver, it is possible to provide navigation updates prior to descent.

This paper provides an overview of the capability of the navigation system in comparison to Earth-based radiometric tracking, showing reduced ground support. Additionally, the lander's descent GNC is simulated to show the landing accuracy enabled by the navigation beacon in orbit. These two use cases provide an overview of the potential applications and performance of the proposed network. Lastly, the paper provides a description of potential orbits for the satellite to operate in to provide services for future lunar missions.

1.1 Lander Mission Overview

This analysis uses the LPL (Lunar Pallet Lander) concept as a baseline mission scenario. The mission is defined in detail in [1, 2, 3]. The objective is to demonstrate precision landing by delivering a payload to the lunar surface within 100 meters of a landing target. Potential landing sites are selected near the lunar pole where water may be present in permanently shadowed regions that could enable future in-situ resource utilization. The LPL is part of a sequence of missions aimed at maturing the necessary technologies, such as lunar precision landing sensors that will enable the next generation of multi-ton lunar payload and human landers. An image of the vehicle is provided in Fig 1 below.

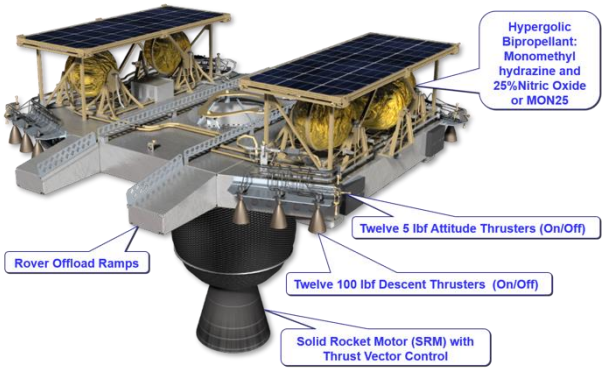

Fig. 1. Lunar Pallet Lander [2]

The LPL uses a combination of liquid propulsion and solid propulsion. The solid stage, composed of an ATK Star 48AV Solid Rocket Motor (SRM), is used for the breaking burn, and it is jettisoned after SRM burnout. The liquid propulsion consists of twelve pulsed thruster descent engines, 100 lbf each, three on each of the four corners of the vehicle, as shown in Figure 1 below. The liquid engines use a hypergolic bipropellant: a Monomethylhydrazine (MMH) as fuel, and 25% nitric oxide (MON25) as oxidizer.

1.2 LPL Trajectory Overview

The LPL mission design assumes a ride on an Evolved Expendable Launch Vehicle (EELV) class vehicle. With the LPL as a primary payload, the mission design is greatly simplified, since the lander can fly into a direct descent to the lunar surface. Therefore, after the Trans Lunar Injection TLI burn, provided by the EELV, the LPL separates from the upper stage of the launch vehicle, as shown in the mission summary in **Error! Reference source not found.**. After system checkout and sun-pointing, the LPL will perform Trajectory Correction Maneuvers (TCMs) to "clean" any TLI insertion dispersions. The mission currently budgets a total of 25 m/s of deltaV for all TCMs. After TLI, and any needed TCMs, the LPL cruises for approximately for 4 days before initiating the breaking burn with the SRM. The LPL trajectory is optimized, to account for SRM performance variations due to solid propellant temperature, **Error! Reference source not found.**, and navigation uncertainties during the SRM burn that could bias the trajectory as much as +-6 km in crossrange and downrange [1, 2]. After the solid burn is completed, a short coast of 30 seconds allows the vehicle to maneuver to its optimal liquid descent burn orientation. The final liquid burn is decomposed on three phases. The first phase targets an altitude of 200 meters above the lunar surface, and a descent velocity of 10m/s [4]. Then, the second phase is a vertical descent from 200 meters down to 10 meters, with a linear ramp down in descent velocity to 1 m/s. A final descent phase is performed at a constant velocity of 1 m/s until touchdown.

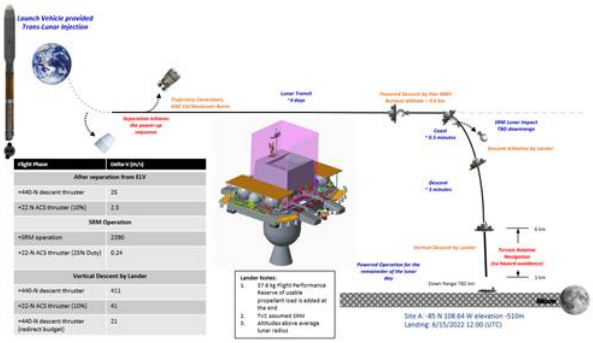

Fig 2. LPL Mission Profile [3]

2. Mission Concept of Operations

Over the next several years, a host of landers similar to LPL will be heading towards the lunar surface to demonstrate high precision and large mass capabilities. These transfers offer an opportunity to piggyback other assets and help to improve cislunar capabilities. Additionally, as more missions continue to operate in this locale, the need for in-situ capability, specifically regards

to communication and navigation will also continue to grow. One approach to address this is to place assets in orbit or on the surface via these technology and science missions to start building out the infrastructure.

2.1 Cubesat Follower Design

The fastest path to flight is to take advantage of the maturing cubesat community, with continuing expansions out into deep space, being demonstrated through the Secondary Payloads on the SLS Artemis I flight [ADD REF]. This approach has also already been successfully implemented and operated for Martian missions. Recently, NASA/JPL landed Insight on the surface of Mars. This mission included two companion spacecraft MarCO-A and MarCO-B, whose primary mission was two-fold: demonstrate the capability for cubesats to operate in deep space, and provide a communication relay for high-rate data collection during the lander's descent operations [6].

This research assumes a similar architecture, but expands the functionality of the cubesat to include built in navigation functionality and onboard propulsion capability to enter into a lunar orbit for extended support of lunar operations, providing coverage across the moon. In order the reach the lunar environment, the cubesat is launched along with the LPL within its deployer. During cruise to the lunar sphere of influence the payload is deployed, allowing time for ground control to verify its operation, and the onboard system to get an initial fix based on the LPL state at deployment. In order to minimize onboard propellant usage, this activity is planned to happen late in the trajectory, after any trajectory corrections are performed on the lander stage.

To provide local navigation support with minimal operational support, the vehicle hosts the NASA/GSFC Navigator GPS receiver [7] which has recently achieved record high-altitude GPS observations on the Magnetospheric Multiscale Mission (MMS) spacecraft. Other studies have demonstrated the capability of this receiver to autonomously navigate using GPS at distances as far out as the moon. In order to integrate with the current version of Navigator hardware, the spacecraft will be on the larger side of cubesats, with an expected 12-24U profile. This technology is enabling force for this spacecraft, allowing it to maintain its own state (time, position, and velocity) to high accuracy. Having this knowledge onboard allows the spacecraft as a navigation beacon to provide support to other vehicles either approach cislunar space, on the surface of the planet, or traveling to/from locations in lunar regime.

2.2 Cross-link Navigation Approach

With this onboard knowledge, the spacecraft can act as a known reference point for other vehicles. This can be achieved by multiple methods. These methods can include radiometric ranging approaches such as that descried in [8, 9] where a spacecraft generates a ranging tone similar to that used in ground-based ranging. This would typically be implemented in a two-way ranging implementation where the signal is transmitted by the traveling spacecraft and retransmitted back by the reference spacecraft. Similar to ground-based operations, the receiving spacecraft can observe a change in phase of the underlying tone to measure a distance the signal has travelled. Additionally, Doppler observation of the return frequency can be used to determine how the relative change in range between the two vehicles.

An alternate approach is to embed navigation data into communications packets sent between the two spacecraft. This assumes that both spacecraft have relatively accurate onboard timing knowledge and well-calibrated software to allow for high precision time delays. Recent advancements in compact timing sources, such as the Deep Space Atomic Clock [10] and the Space Chip-Scale Atomic Clock, provide the accuracy needed for this navigation approach. This technique forms the basis of the Multi-spacecraft Autonomous Positioning System [11] that has been testing on the International Space Station in 2018 [12] and is being implemented in the form of a lunar beacon using a Space Chip-Scale Atomic Clock [13] as part of the Lunar Node – 1 payload, planning to fly in 2021 onboard a commercial lunar lander.

This study assumes a ranging capability built into the communication system of LPL with a corresponding node integrated into the follower/beacon cubesat. The analysis herein focused on the required measurement capability to focus on the performance of the proposed system with future work to study this architecture in hardware-in-the-loop analysis on flight systems.

2.3 Trajectory Design

As provided in section 1.2, LPL is assumed to be placed on a direct translunar orbit with a limited mission duration. As mentioned, this analysis assumes the follower cubesat deploys prior to the vehicle approaching the lunar Sphere of Influence to limit orbital dispersions between the two spacecraft. The baseline mission for inserting into a polar orbit is shown in Fig 3 below. This plot is shown in a lunar fixed frame, showing the approaching spacecraft and its insertion into a local orbit. Figure 4 provides more details on the evolution of the polar orbit over time. For this scenario, several orbits were considered in terms of altitude and inclination to assess coverage of the hosting lander as well as requirements on propulsion sizing. Another option considered in trajectory design was looking at lunar flyby orbits. As opposed to the spacecraft entering a fixed orbit, the constraint is to pass above the lunar surface with enough energy to fly heliocentrically and potential fullfill

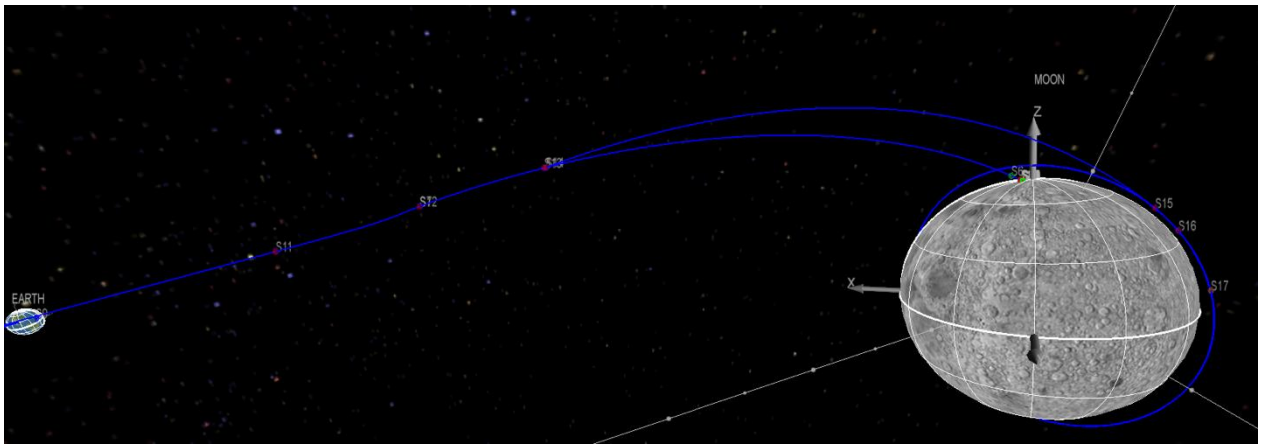

Fig. 3. Integrated trajectory showing LPL Lunar transfer and Follower insertion into polar lunar orbit

another mission, or only provide support for the descent of the spacecraft.

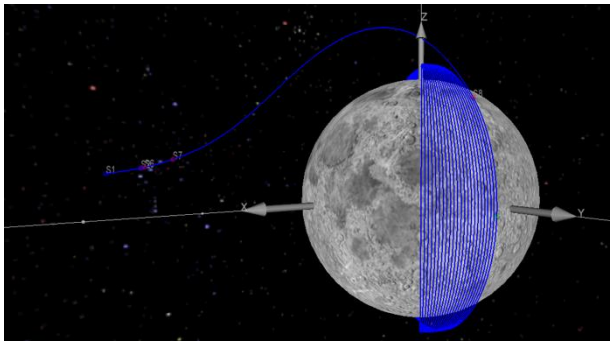

Fig. 4. Follower trajectory from deployment to orbit

4. Vehicle Sizing for Lunar Orbit Insertion

4.1 Trajectory Optimization

As proposed in this architecture, the mission will take advantage of a follower cubesat to house the Navigator receiver and provide relative navigation observations. This spacecraft will need to perform braking and transfer burns in order to remain in a defined stable lunar orbit, with the necessary ΔV dependent on the desired orbital states. In order to provide insight into the design mechanics for any such potential mission, a ΔV study was performed using Copernicus [14]. The analysis that the CubeSat in question was on a lunar approach trajectory taken from a trajectory originally created for the LPL mission, with the reference vehicle being taken from the LPL mission 6U (assuming 1U is equivalent to 1kg) CubeSat with a specific impulse of 292.6s. For simplicity, all evaluated missions were assumed to end in a circular orbit at a lunar altitude of either 100 or 200km and at an inclination of either 0°, 45°, or 90°. This represented a broad swath of simple orbits for which a potential mission could aim.

Using Copernicus, each of the 6 evaluated missions shared a common initial segment as adapted from the LPL mission input deck. This state was chosen to be a near entering the Lunar Sphere of Influence. The main difference between the 6 input decks was the destination orbit defined via the Keplerian elements of semi-major axis, eccentricity, and inclination as previously stated. Each mission segment inherits from the previous segment and included an optimizable impulsive burn followed by a coast for the remainder of the segment. The SNOPT algorithm was used to optimize the final solutions by minimizing the total ΔV required. It was found that the initial design of up to 5 mission segments was insufficient for Copernicus to find viable solutions, with the first and final segments being coasting segments with variable segment times and the remainder being the braking burn for lunar capture, the burn to go from the initial lunar orbit to a potential intermediate orbit, and a final burn to put the spacecraft into the destination orbit. Empirical testing found that at least 9 segments were required, with an optimal trajectory having several small burns with magnitudes less than 1cm/s and one or two burns consuming the majority of the total ΔV for the mission. After an optimal trajectory was found for each mission, the total ΔV was recorded as a baseline for the evaluation of potential propulsion systems. The total ΔV budget results are shown in Table 1 and Table 2.

Table 1. 100 km Altitude Insertion Orbit Requirements

Inclination:	0°	45°	90°
ΔV_1 (km/s)	0.000	0.000	0.000
ΔV_2 (km/s)	0.005	0.009	0.002
ΔV_3(km/s)	0.071	0.079	0.082
ΔV_4 (km/s)	0.002	0.000	0.049
ΔV_5 (km/s)	0.000	0.000	0.002
ΔV_6 (km/s)	0.000	0.000	0.001
ΔV_7 (km/s)	0.069	0.075	0.002
ΔV_8 (km/s)	0.837	0.845	1.180
ΔV_9 (km/s)	0.000	0.000	0.000

ΔV_Total (km/s)	**0.984**	**1.010**	**1.320**

Table 2. 200 km Altitude Insertion Orbit Requirements

Inclination:	0°	45°	90°
ΔV_1 (km/s)	0.000	0.000	0.000
ΔV_2 (km/s)	0.002	0.030	0.000
ΔV_3(km/s)	0.100	0.000	0.003
ΔV_4 (km/s)	0.003	0.000	0.001
ΔV_5 (km/s)	0.005	0.000	0.000
ΔV_6 (km/s)	0.006	0.297	0.053
ΔV_7 (km/s)	0.036	0.543	0.000
ΔV_8 (km/s)	0.794	0.000	0.751
ΔV_9 (km/s)	0.000	0.000	0.000
ΔV_Total (km/s)	**0.946**	**0.870**	**0.809**

4.2 Delta-V Requirements and Propulsion Feasibility

Once the ΔV requirements for these orbits were determined, it is necessary to determine any other required performance information to inform the down-selection of a propulsion system for a mission. Given the coarse state of the analysis, the required ISP for a given burn was the only independent performance parameter that could be determined. It is possible using the Tsiolkovsky equation (Eq. 1) to solve for the ratio of propellant mass to dry mass (Eq. 2), referred to as the mass ratio for the rest of this document. By constraining the mass ratio to equal 2, the minimum necessary ISP to successfully insert the vehicle into the desired lunar orbit can be calculated (see Equation 3).

$$\Delta V = I_{SP} * g_{ref} * \ln\left(\frac{m_{prop} + m_0}{m_0}\right) \quad (1)$$

$$m_{rat} = \frac{m_{prop} + m_0}{m_0} \quad (2)$$

$$I_{SP}^{min} = \frac{\Delta V}{g_{ref} * \ln(m_{rat})} \quad (3)$$

From Eq. 3, the minimum acceptable ISP is directly proportional to the required ΔV and inversely proportionate to the natural logarithm of the mass ratio. This process informs an initial choice of a portfolio of propulsion systems that could be utilized for a given mission before a more detailed analysis can be performed.

Given the design point ΔV values calculated in the previous section, the minimum required ISP for each mission was calculated using Eq. 3 and assuming that the reference gravity was 9.81 m/s^2. The results are shown in Table 3 and Table 4. After these minimum required ISPs had been determined, the propellant mass and mass ratios were calculated for permutations of the six reference ΔV values and ISP values ranging from 1s to 2048s. The resulting distributions were used to create contour plots with the ISP ranges for various propulsion systems overlaid for clarity. Figure 5 provides insight into the propulsion sizing, showing the trend between ISP and mass fraction. Figures 6 and 7 show the total propellant mass required for a 12U and 24U platform to inform vehicle design decisions between technology readiness, mass required, and total system mass.

Table 3. ISP for 100km with Mass Fraction of 2

Inclination	0°	45°	90°
ΔV (km/s)	0.92	1.29	0.85
Min. ISP (s)	135.0	190.0	124.0

Table 4. ISP for 200km with Mass Fraction of 2

Inclination	0°	45°	90°
ΔV (km/s)	0.89	1.39	0.82
Min. ISP (s)	131.0	205.0	120.0

Optimizing the trajectories via Copernicus found that the ΔV required for the evaluated missions ranged between 0.81 and 1.32km/s in total. Using Eq. 3 to solve for the minimal ISP for each of the missions generated a range from 120 to 205s for a mass ratio of 2. Cold gas systems do not meet this required ISP performance, although all but the lowest performing hydrazine and green propulsion systems exceeded 205s. The hydrazine and green propulsion systems permit mass ratios from 2 to just less than 1.5 – meaning that the propellant mass would be approximately half that of the dry mass. The remaining categories of propulsion systems (ion, pulsed plasma or vacuum arc, electrospray, and Hall Effect thrusters) enabled mass ratios of less than 1.25.

Assuming that the mass ratio must be less than 2 for any given mission, the ISP must be at least 205s for any mission analyzed herein. Based on the information found in Table 4-1 of [15], this means that all evaluated categories of propulsion systems except those using cold gas are viable options for lunar missions given the range of ΔV values presented here. In particular, any propulsion system with an ISP exceeding 700s would permit a mass ratio of 1.25 or less for a given mission with a ΔV less than 1.3km/s. These rough findings should enable further, more detailed analyses on the performance of specific propulsion systems, such as a study with the modeling of finite burns instead of impulsive maneuvers for a given mission.

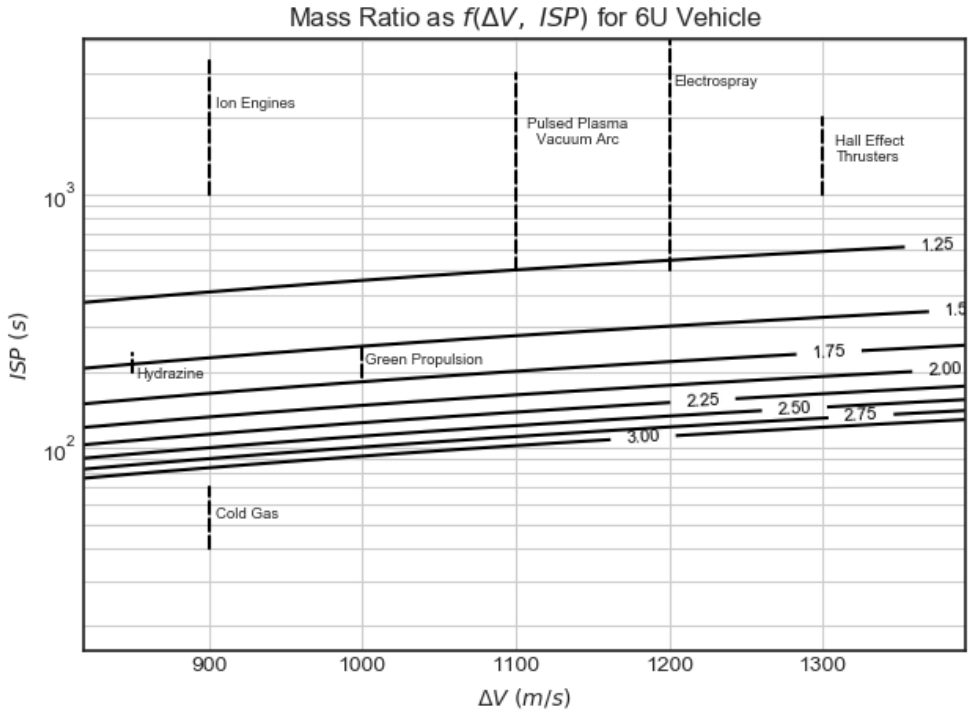

Fig. 5. Ratio as a Function of Required ΔV and ISP Values with ISP ranges of Different Propulsion Systems

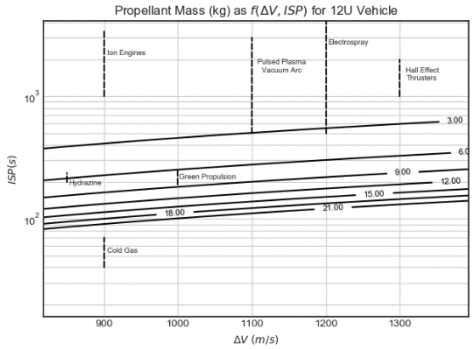

Fig. 6. Contours of Propellant Mass as a Function of ΔV and ISP of 12U Vehicle.

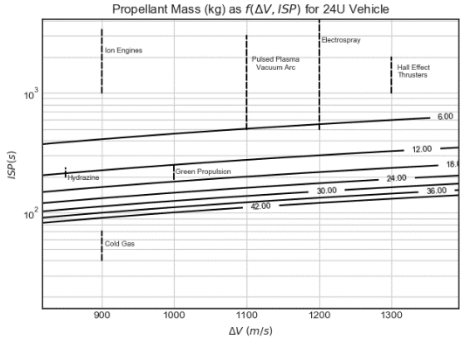

Fig. 7. Contours of Propellant Mass as a Function of ΔV and ISP of 24U Vehicle.

5. Performance of Navigator in Representative Orbits

Given the trajectory design of the LPL and feasibility of the follower cubesat, analysis was performed using the Goddard Enhanced Orbital Navigation System (GEONS) software [16] to understand its capability. The focus of this section is to provide insight to the navigation capability using the Navigator receiver along the mission profile. Weak signal GPS and accelerometer-like performance of maneuver knowledge are the only sensors examined in this study. The weak signal GPS performance is based on the observed Magnetospheric Multiscale Mission satellite GPS hardware performance while the accelerometer performance is modelled loosely off of Orion IMU specifications (error in impulsive DV of 0.15% of maneuver). GPS measurements (L1 pseudorange) were assumed to be available every 30 seconds.

The GPS signal simulation model is based on a model of the MMS-Navigator GPS receiver augmented with a ~0.5 m diameter 14 dBi high-gain antenna, and realistic GPS link model calibrated for consistency with the on-orbit MMS GPS signal strengths. This model uses the recently released in-orbit measured per-block mean transmit patterns from the GPS Antenna Characterization Experiment (ACE) project [17] and a GPS yaw model to accurately reproduce C/N0 and visibility due to GPS transmitter sidelobes which can be the majority of visible signals in high altitude applications. The GPS simulation setup is as in [7], where further detail can be found.

The following equation is used to model the GPS-to-receiver link signal-to-noise-ratio:

$$C/N_0 = P_T + G_T(\varphi, \theta) - 20\log(4\pi/\lambda_{L1}) + G_R(\varphi, \theta) - L_{pol} - 10\log(kT_{sys}) - R_{loss} \quad (4)$$

where λ_{L1} is the GPS L1 carrier wavelength, k is the Boltzmann constant, and the remaining parameter definitions and values are summarized in Table 5. Since the proposed design of the receiver front-end is very similar to the MMS-Navigator receiver, the MMS-calibrated link parameters are used to simulate the GPS-to-receiver signal strength in the analysis of the trajectories.

Table 5. Calibrated Link Parameters from analysis of MMS-Navigator GPS and high-altitude MMS flight data

Link Parameter	Value
Antenna Temperature T_a	34 K
System Temperature T_{sys}	132 K
Implementation Loss R_{loss}	1.7 dB
Polarization Loss L_{pol}	1 dB
Block II/IIA P_T	17.9 dBW
(max EIRP)	(31.6 dBW)
Block IIR P_T	17.3 dBW
(max EIRP)	(29.2 dBW)
Block IIRM P_T	18.8 dBW
(max EIRP)	(32.1 dBW)
Block IIF P_T	16.2 dBW
(max EIRP)	(29.5 dBW)

The transmitter antenna gain patterns G_T were provided as a function of off-boresight angle (elevation) and azimuth in the ACE datasets. For the receiver gain pattern G_R, we used a model of the composite MMS receive pattern that provides peak gain of approximately 6.3 dBi in the ecliptic plane, but with the peak gain adjusted to 14 dBi to model an Earth pointed high-gain antenna (e.g., ~0.5m diameter dish or multi-element array).

A maximum of 12 GPS pseudorange (PR) measurements are simulated every 10 s with a simple unbiased additive random error model of 10 m below, and 4 m above, a 40 dB-Hz "strong signal" threshold (all 1σ). In addition, ionospheric delays can be included in the simulated PRs, but are not in these studies. A 32 GPS SV constellation is modelled using a broadcast ephemeris file from 2017, but advanced to the current date. GPS visibility is assessed based on the GPS link model given in (4) above, Earth and Moon occultations, and a probabilistic model of the receiver's acquisition and tracking performance with a sensitivity of 23 dB-Hz.

Several additional configuration parameters were used in defined the analysis scenario. The onboard clock model utilized was based on a SpectraTime Rubidium Atomic Frequency Standard (RAFS) clock [citation to datasheet] – one example of a commercially available space qualified atomic clock---which was also used in [7]. The filter was configured to solve for the position, velocity, time bias, time bias rate, and time bias acceleration. The process noise model utilized is 1e-14 (m^2/s^2) – in line with previous studies on Gateway and MMS navigation.

5.1 Navigation along Lunar Transfer Trajectory

The first trajectory segment studied is a lunar transfer trajectory from Low Earth Orbit to the lunar environment. Figures 8 and 9 show the position and velocity errors from a single simulation run, respectively, each separated into range and lateral components. In both position and velocity the range errors are dominant due to challenges in separating range and clock errors using GPS pseudoranges at high-altitude, without significant dynamics. Further discussion of this phenomenon is provided in reference [7]. Nonetheless, position errors remain below 60 m and velocity errors under 0.5 mm/s each channel.

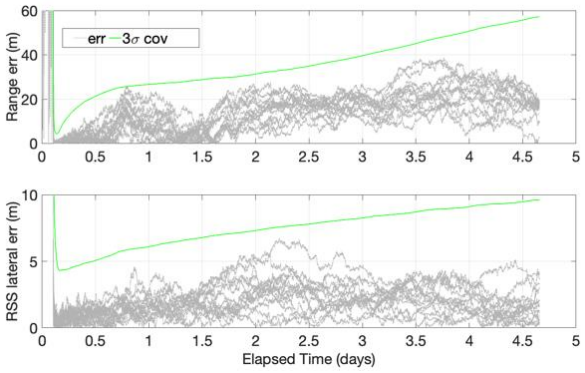

Fig. 8 Position Errors and 3-Sigma Uncertainty from Covariance – LEO to Lunar

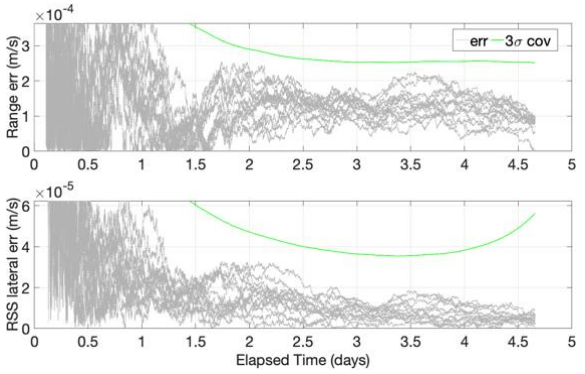

Fig. 9. Velocity Errors and 3-Sigma Uncertainty from Covariance – LEO to Lunar

Figures 8 and 9 show an initial convergence period followed by gradual error growth with time and distance from Earth. This is consistent with expectations; as the

spacecraft travels farther from the Earth, the number and geometric diversity of the available GPS signals both degrade. This results in the corresponding degradation of the navigation solution. A 100 run Monte Carlo was performed in order to validate the results presented in the single run case. The results of this analysis showed the 3-sigma root-covariance bounded the dispersed cases, providing confidence in the simulation and filter configuration.

5.2 Navigation during Insertion into and Operation in a Polar Orbit

The second trajectory examined for LPL begins at the sphere of influence of the Moon (SOI), performs 2 lunar orbit insertion (LOI) burns, and orbits the Moon in a 200 km circular low lunar orbit (LLO). For this trajectory, and for simplicity in running the GEONS simulation, the GPS measurement update rate was set to follow the variable time step in the trajectory file (ranging from 1.5 hours to fractions of a second). While this deviates from how the GPS would be run on board, with a regular 10-60s update rate, it turns out to not drive performance. The rest of the navigation assumptions are unchanged from the previous trajectory.

Typical position and velocity results from a single run are shown in **Error! Reference source not found.** and **Error! Reference source not found.**, respectively, again separated into range and lateral components. Once inserted into the LLO, the steady state errors appear to be on the order of 50 m in position and less than 5 cm/s in velocity. In this case, the lateral errors are dominant. The strong dynamics of the LLO enable the filter to resolve the clock as seen in Figure 12, at which point GPS provides excellent range information, while the lateral errors are limited by available geometry of GPS signals received at the moon.

It is also important to note that this orbit has a 90-degree inclination with respect to the Moon and is oriented such that there is near-continuous visibility from user to the GPS constellation over the simulation period. Navigation performance is limited by the number of the GPS SVs that can be acquired and the associated GDOP. In the LLO, the number of satellites drops to zero on occasion due to poor signal availability and occasional occultations. These outages result in periodic spikes in covariance as witnessed in **Error! Reference source not found.**.

Prior to the LLO insertion the errors larger and are range/clock dominated and reach 200 m or more. Whiel on a continuous earth-moon trajectory, the filter would be converged upon reaching the SOI, this analysis started with the same initial error covariance as the LEO-to-Lunar analysis and did not utilize a converged a-priori covariance. Therefore, in the region from SOI to LLO, slower convergence time is observed in the navigation state due to the weak dynamics. As the spacecraft approaches and enters the LLO, dynamics from the Moon's gravity assist the filter in converging onto a solution. To further illustrate this, **Error! Reference source not found.** reveals that in the presence of strong dynamics, where significant correlations between the state elements exist, the filter can resolve the clock state to much higher accuracy.

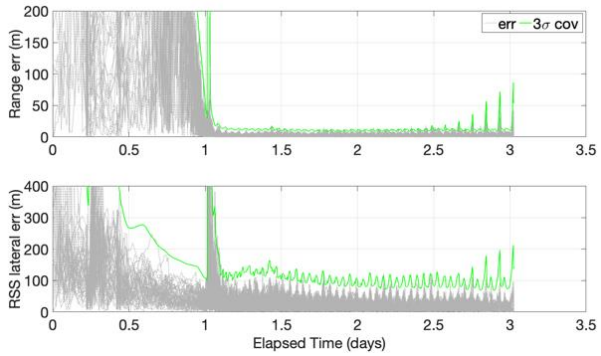

Fig 10. Position Errors and 3-Sigma Uncertainty for Cruise and Polar Orbit

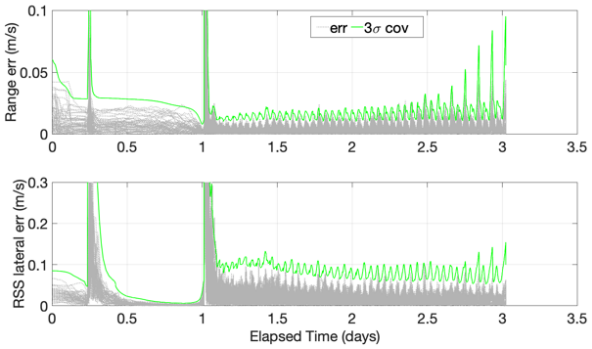

Fig. 11. Velocity Errors and 3-Sigma Uncertainty for Cruise and Polar Orbit

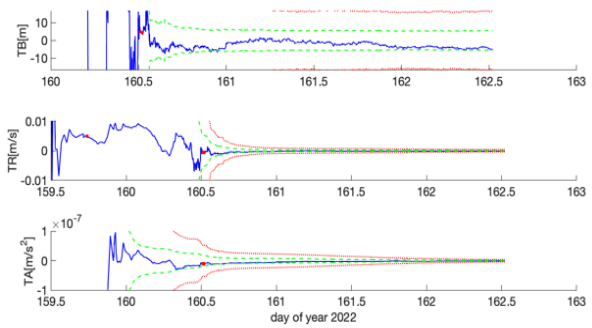

Fig. 12. Clock Estimation at Orbit Insertion

While it may be tempting to attribute the initial poor performance on the variable time step in the simulation (large time steps are utilized in the SOI through LOI maneuver and shorten in the LLO), dynamics is the

largest contributing factor to the initial difficulties of the filter to resolve the state. To illustrate this, the filter is shown to converge at the second LOI maneuver where the time step is on the order of 35 minutes. This conclusion is consistent with the previous analysis (LEO to Lunar) where the navigation state degrades in the cislunar space. However, it is expected that more frequent GPS measurement availability would improve the initial convergence and steady state errors.

5.3. Navigation during Insertion into and Operation in an Equatorial Orbit

The third trajectory examined for LPL begins at the SOI, performs 2 LOI burns, and orbits the Moon in a 200 km circular equatorial LLO. Similar analysis in GEONS was performed as in the previous section to assess GPS performance. Figure 13 and Figure 14 show the position and velocity errors from this run, respectively. The performance is similar to the Polar Orbit case, except here there are periodic spikes in the errors and especially covariance corresponding to occultation of the GPS constellation by the moon.

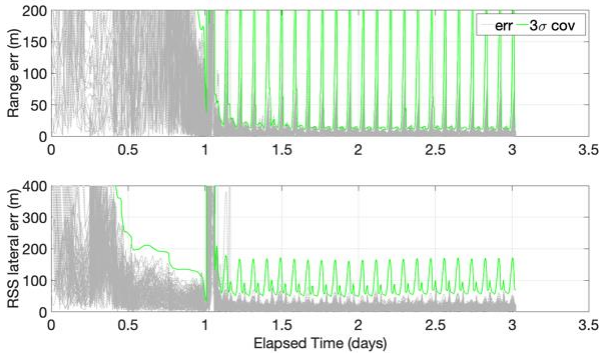

Fig. 13. Position Errors and 3-Sigma Uncertainty During Cruise and Insertion into Equatorial Orbit

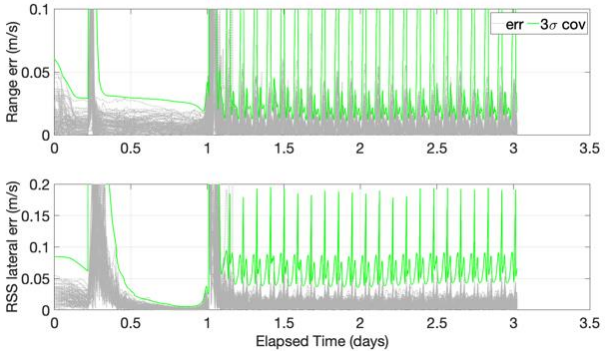

Fig. 14. Velocity Errors and 3-Sigma Uncertainty During Cruise and Insertion into Equatorial Orbit

6. Integrated Vehicle Performance

The results of the previous section were used to provide analysis of how ranging measurements can be used to support navigation between the two spacecraft. This analysis focused on two aspects of the mission: ensuring adequate state knowledge prior to beginning lunar descent (defined by the solid rocket motor to begin the de-orbit), and for use in verifying landing location. An additional area of support can be to provide observations during landing, but that is the focus of forward work to assess.

6.1 Cross-vehicle Updates During Cruise

To assess performance during cruise operations, a covariance analysis approach was used to propagate state uncertainty along the cruise trajectory to lunar de-orbit. For this analysis, a state transition matrix was used to capture error growth due to orbital mechanics. To simplify the analysis (similarly to the GEONS assumptions above), effects such as SRP were not included. The only forces included are due to Earth and lunar gravity terms to first order. A 1 second time delta was used to propagate the vehicle error dynamics. For this analysis, the simulation starts assuming an external state update with 100 meters and 0.1 m/s one-sigma uncertainty.

The first part of the analysis focuses on utilizing only DSN observations as part of the flight operational sequence. For this analysis, the ground-calculated orbit determination solution is provided to the spacecraft's onboard filter as a measured position and velocity. For these measurements, the uncertainty is again tied to the 1-sigma initial errors used at the start of the simulation. These updates were first provided once a day to show comparison to the primary navigation requirement during the LPL's cruise: position knowledge within each axis to 100 m and velocity knowledge to within .1 m/s. This level of accuracy is required to allow the vehicle to do an efficient braking burn with the SRBs and to accurately insert into a descent trajectory. The results of this analysis are given below in Figures 15 and 16, which show 3-sigma expected bounds from the covariance analysis over the trajectory.

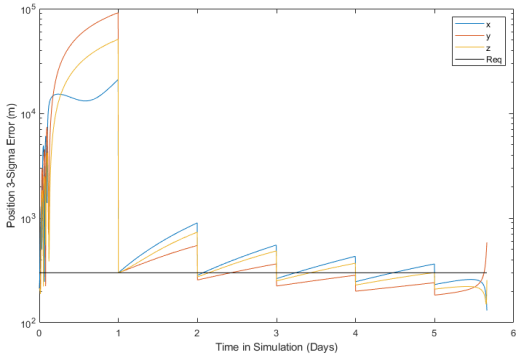

Fig. 15. Position 3-Sigma over Trajectory

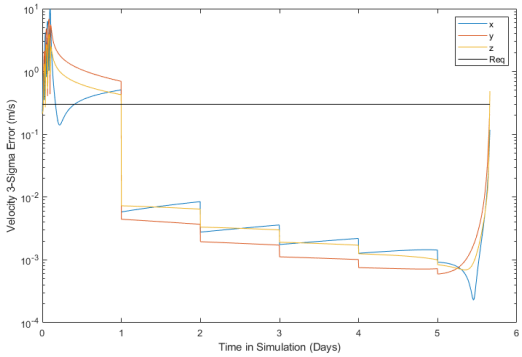

Fig. 16. Velocity 3-sigma over Trajectory

From both of these analyses it is shown that daily DSN updates with the provided accuracy are adequate to provide the required knowledge at the start of LPL descent operations. At the end of the trajectory, as the vehicle begins its approach the moon, the gravity forces greatly increase, causing an increase in the effect of time on the propagation of the errors. While both of the trajectories show slightly above the requirement in terms of velocity in one-axis, this can easily be tuned by moving the timing of the last observation, which in this simulation was still greater than half a day out. To provide more insight into the sensitivity to external updates, the analysis was repeated with varying frequencies of external updates, the integrated 3-sigma position and velocity uncertainty is given in Figures 17 and 18.

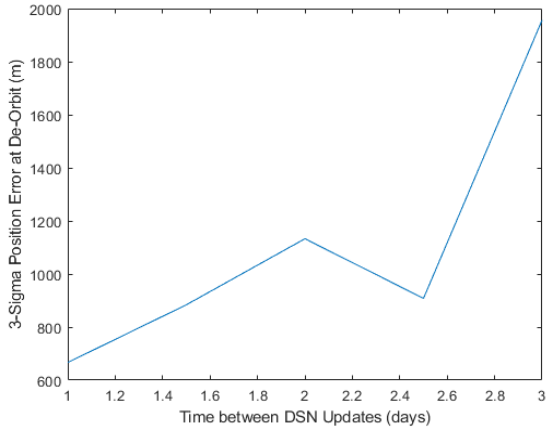

Fig. 17. Effect of DSN Update Rate on Total Position Uncertainty at Start of Descent

These results show a strong sensitivity to the time between external measurement updates, and a need for an update fairly close to the time of de-orbit in order to meet landing accuracy requirements. An alternate approach, and the focus of this work, is to assume the use of ranging measurements from a follower spacecraft. This was assessed by modelling the updated as a measurement of range between the two spacecraft. For the covariance filter, the derivative of the range equation to individual position states of the spacecraft is used to capture the measurement sensitivity as part of the update equation.

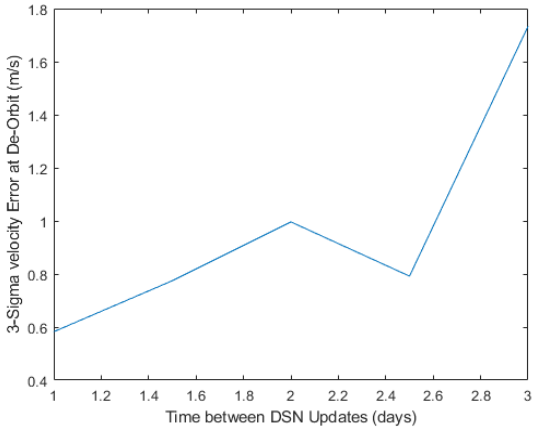

Fig. 18. Effect of DSN Update Rate on Total Velocity Uncertainty at Start of Descent

Assessing the ability to measure the range must take into account multiple error sources. In this case, the measurement uncertainty is due to both the follower spacecraft's knowledge of its own state as well as the ability for the LPL to measure its range to the follower. For this analysis, a time-delta of 5 minutes was assumed for inter-spacecraft ranging measurements. At each of these intervals, the navigation analysis performed above was used to capture the onboard accuracy of its solution. This was taken from the covariance of the Navigator-based solution as a function of time described in Section 5.2. This value was summed with an uncertainty based on expectation of the range measurement itself that was then used to capture the total uncertainty of the measurement.

To assess the navigation capability at the start of descent, two analysis trades were completed. The focus is to assess the sensitivity to measurement errors in the range observable as well as the effect of knowledge of the follower's onboard state. The baseline architecture includes a method for this data to be shared between the two systems as part of the ranging measurement mechanism. This analysis also used a covariance-based approach, and traded five possible levels of measurement error [1, 10, 100, 1000, 10000] meters 1-sigma and assessed two cases, with and without the effect of the autonomous navigation solution on the follower spacecraft. Figure 19 and 20 below show the results of this analysis.

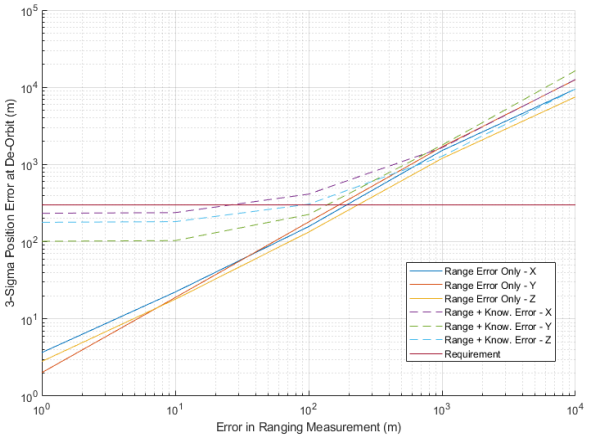

Fig. 19. Position Uncertainty as a Function of Measurement Error and Knowledge Uncertainty

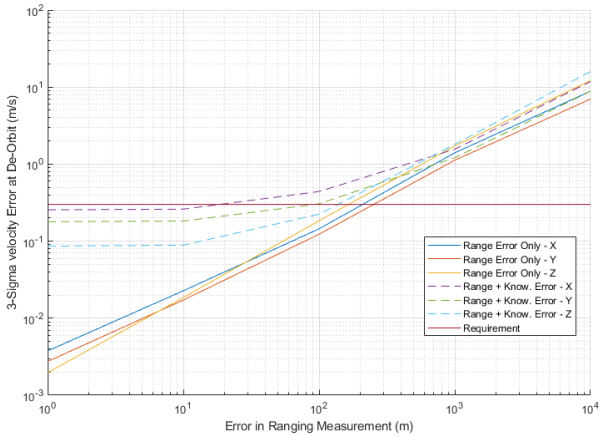

Fig. 20. Velocity Uncertainty as a Function of Measurement Error and Knowledge Uncertainty

Two key trends are visible in this data. First of all, assuming no knowledge errors, the ability to navigate the LPL correlates strongly with the error on the ranging measurement. This is as expected, and the system cannot determine its state any better under these dynamics than the uncertainty in the observation itself, though the many observations provide a high level of insight into the velocity terms. The modelling of stochastic accelerations in the dynamics terms would reduce this estimation accuracy.

A second trend is shown in the flattening of LPL knowledge accuracy due to the effect of the beacon's uncertain state. This is shown in the dashed lines in the two figures. The follower's accuracy is limited by the performance of the GPS receiver along its coast trajectory. As such, at small measurement errors, the total uncertainty is more driven by orbital uncertainty than ranging errors. The results show that with the expected orbital determination knowledge, ranging measurements with 100 meters one-sigma uncertainty get the system very close to its requirements, with 10 meters easily providing additional performance. Additionally, all of these simulations assumed no external state updates to the LPL or follower satellite during the simulation. The results of these studies show the potential for this system to be used to support autonomous state determination for LPL prior to its descent manuevering. The next step of this analysis is to perform Monte Carlo simulation of the cruise trajectory with expanded models to improve the fidelity of the modelled truth dynamics as well as to test the proposed ranging mechanisms to verify their capability. Additionally, refinement of the LPL onboard filter and integration with existing sensors could further improve its state knowledge.

6.2 State Update during Descent

With insertion into a polar orbit, the spacecraft maintains the LPL in its communication line of sight during the complete descent profile. Over the course of the large de-orbit maneuver navigation errors will grow. Currently, the lander navigation design relies on a broad suite of precision navigation sensors to enable high accuracy landing while under powered thrust. The follower spacecraft will be overhead during the descent manuever, allowing it to fullfill its role in capturing high rate data during descent. A plot showing the relative range for both polar and equatorial bound spacecraft is shown in the Figure 21 below. With the inclusion of ranging to the follower spacecraft, it is possible to provide an additional measurement reference. Future trades will assess the performance increase during the landing portion of flight and evaluate various sensor combinations to assess an updated vehicle navigation suite.

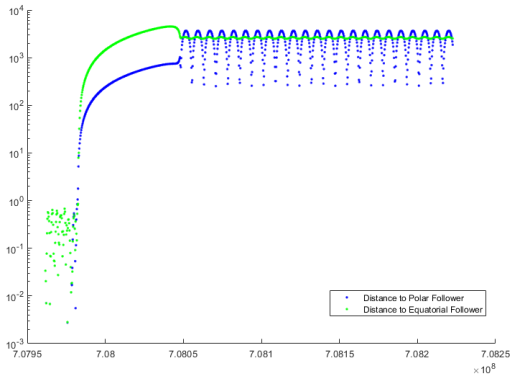

Fig. 21. Range between LPL and Follower Spacecraft from Deployment through Several Orbits

The caveat to this range information is that it doesn't take into account whether the follower is within the line-of-sight of the LPL once it's landed on the surface. To assess this, a constraint was applied to angle between a

pointing vector from the landed vehicle to the orbiting spacecraft and the local vertical. This was use to model the local terrain blocking line of sight between the two elements. For the initial analysis, a 75 degree constraint and the results are seen in Figure 22 with the ground passes shown in Figure 23. As seen, the equatorial cubesat is never in view, and actually drops out prior to landing. The Polar cubesat is visible through the entire descent and then is visible again on a cycle of 10 minute passes every 2 hours. This enables continued coverage, landing verification, and communication support over an extended mission. Other orbits were used in the sizing analysis can be used to optimize desired post-landing ground-coverage.

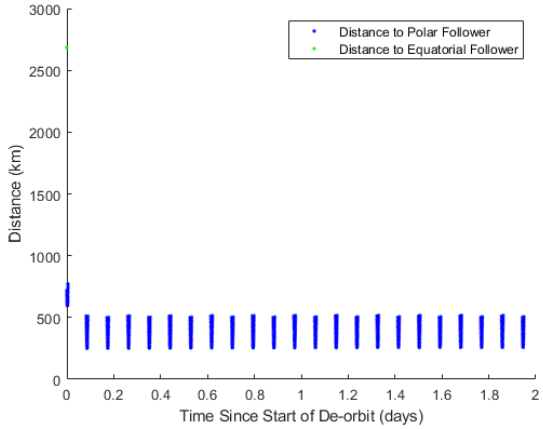

Fig. 22. Range between LPL and Follower Spacecraft with 75% Elevation Cutoff Applied

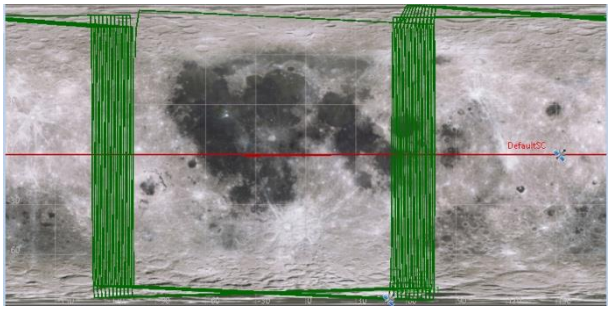

Fig. 23 Orbital Coverage of Spacecraft (Red = Equatorial Orbit, Green = Polar Orbit)

6.3 Landing State Verification

The above section provides insight into the post-landing surface potential of the now-orbiting cubesat. The first application of this vehicle would be to support ground site determination and verification. Landers such as LPL have a requirement for precision landing, with the ability to land within 100 m of a prescribed target. In order to assess post-flight performance, ranging between the landed vehicle and the orbiting spacecraft can be used to update its onboard state via external measurements. Other approaches focus on using DSN or retro-reflectors to generate range observations from Earth to the lander.

This analysis looks at using ranging measurements as an input to a landing determination algorithm onboard the lander. In order to assess, a nonlinear least squares algorithm was implemented to iteratively solve for the lander position. The input to the algorithm is the initial landing estimate and a series of observed ranges. The primary drivers now are the accuracy of the measurement (as seen above) and the overall duration of the measurement campaign. For this study, ranging errors of .1, 1, 10, 100, 1000 m were considered along with using up to the 11tth ground pass (equating to about a day's worth of observation data). Monte Carlos were completed to assess random noise sources in the ranging measurement and initial state errors. For each combination of number of passes used and 1-sigma range measurement, 100 cases were assessed to determine the mean of the magnitude of the errors for each case. This is intended to get provide insight into key system sensitivities. The plot below in Figure 24 shows a contour comparing number of passes (as shown in Figure 22) on the y-axis, with the measurement errors in a log scale on the x-axis.

The contours on the plot represent magnitude of the error for that approach. As can be seen in the analysis, the estimation capability is primarily driven by the noise term, but the impact of more passes is clear utilizing more passes can help to reduce errors. It is useful to note that the individual passes are fairly short. If the focus was on ranging to Earth, the vehicle would have essentially constant link availability allowing for a much greater observation duration.

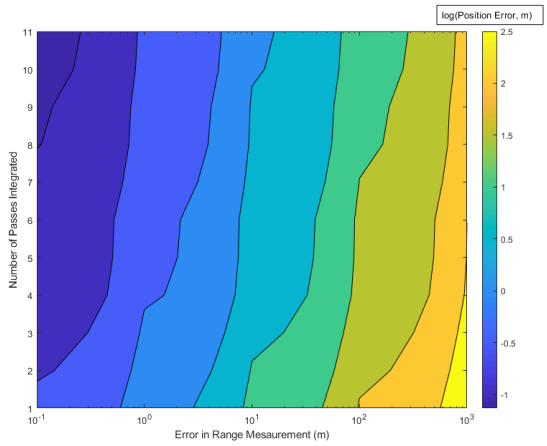

Fig. 24. Ground Determination Accuracy Sensitivity to Observation Time and Measurement Error

Similar to the analysis above, it is important to consider the effect of the onboard vehicle's knowledge capability in determination of the lander location. This primarily affects the ability for vehicle to model the range measurement. To account for this, the vehicle's

uncertainty was treated as an independent error on the range observation. The covariance data was used to generate an error in each axis at the time of observation. The total offset of the computed range error was then added to the measured value as an additional error. The same trade study was completed as for the previous case and the results are in the Figure 25.

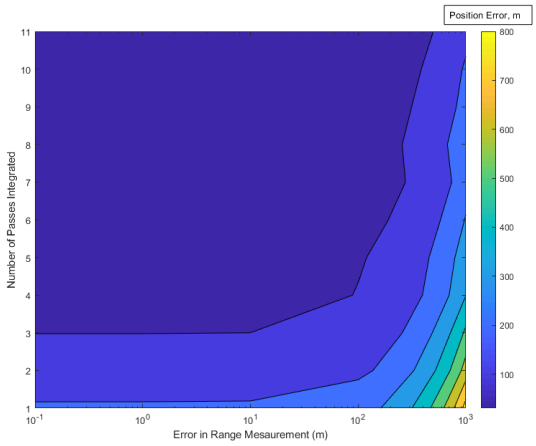

Fig. 25. Effect of Vehicle Knowledge Effects on Ground Determination Accuracy

As shown in the plot above, the knowledge of the follower spacecraft's position has a direct limitation on the ability to determine a ground location. While the effect of increased observation can improve the final knowledge with larger measurement errors, as these decrease the overall capability is limited by the knowledge uncertainty. This also helps to inform a desired ranging accuracy, upon which further refinement would provide minimal return. This represents a very achievable system, and while not providing meter-level accuracy, can provide in-situ observations across a range of applications on the lunar surface and in orbit. Additionally, the implementation of this capability can still support a variety of mission scenarios and traversal of the lunar regime. Further refinement of the state determination algorithm and integration with other vehicle observations can help to further improve the LPL estimate. Although the analysis here focused on a fixed lander position, this architecture can also support operations across the lunar polar, wherever the satellite has a line of sight to. As expanded coverage is needed, additional satellites with this capability can be placed into orbit, or existing assets, re-phased to meet mission needs.

6.4 Continued Operations

With the spacecraft in lunar orbit, it can continue to support operations in the local environment for a variety of other mission scenarios. In addition to providing coverage for surface operations in terms of navigation and communication, it can also support elements ascending from the lunar surface and assist in state determination prior to launch. Similarly, as shown here, the vehicle can act as a beacon to support other incoming spacecraft as well as vehicles traveling between various lunar orbits.

7. Conclusions and Discussion

This research lays out a powerful architecture for enabling a breadth of navigation and communication potential for lunar-focused missions. The integration of the Navigator GPS Receiver onto a lunar cubesat provides a highly accurate timing and navigation reference source for other assets in the region. The mission herein focused on the application of a follower spacecraft flying with a lunar lander. This application exhibited great benefit to both cruise and post-landing phases of flight. This is achieved through helping to maintain an accurate onboard state at high frequency throughout flight, minimizing the need for external ground-based tracking. With this architecture, the lander able to maintain an accurate state up until lunar descent, enabling a high precision landing approach, reducing initial errors.

Furthermore, this analysis has demonstrated the expected capability of the Navigator receiver both during its transfer to the moon and while in lunar orbit. While in lunar orbit, the spacecraft was able to maintain position knowledge of less than 100 meters. With improvements in integration of onboard accelerometer and attitude information, this capability to will continue to be refined. As shown it the analysis, this baseline performance can be used to both support high precision landing verification, as well as potential support of incoming or outgoing vehicles. The analysis presented herein focuses on the transfer during cruise and post-landing legs. The ability of integration of external measurement during planetary descent and ascent is under further study. With this capability for autonomous navigation, lunar vehicles can be designed to accomplish more complicated missions and be able to operate with minimal control from Earth-based mission control. This is increasingly important for the large number of planned lunar missions as part of the Artemis efforts.

Acknowledgements

The authors would like to acknowledge the work and support of the LPL/VIPER analysis and Navigator teams at GSFC and MSFC. Their work and design form the basis of this analysis informed the scope and application of this work. Additionally, the authors would like to thank their management in support of enabling this work and documentation.

References

[1] S. Craig, J. P. Holt, M. R. Hannan, and J. I. Orphee, Mission Design for the Lunar Pallet Lander, AAS/AIAA Space Flight Mechanics Meeting, January 2019. AAS 19-330.
[2] J. W. Jang, S. Bhatt, M. Fritz, D. Woffinden, D. May, E. Braden, and M. Hannan, "Linear Covariance Analysis for a Lunar Lander," AIAA Guidance, Navigation, and Control Conference, AIAA SciTech Forum, 2017. AIAA-2017-1499.
[3] J. Orphee, M. Hannan, et al, Guidance, Navigation, and Control for the NASA Lunar Pallet Lander, AAS Guidance, Navigation, and Control Conference, February 2019. AAS 19-033.
[4] A. R. Klumpp, Apollo Lunar-Descent Guidance", Charles Stark Draper Laboratory, R-695, June 1971.
[5] SLS Secondary Payloads paper.
[6] A. Klesh, et al., MarCO: Early operations of the first CubeSats to Mars, 32nd Annual AIAA/USU Conference on Small Satellites. 2018.
[7] L. Winternitz et al., GPS-Based Autonomous Navigation Study for the Lunar Gateway, AAS 19-096, Proceedings of the AAS 42nd Annual Guidance and Control Conference, February 2019.
[8] E. G. Lightsey, et al., Real-time navigation for Mars missions using the Mars network, Journal of Spacecraft and Rockets, 45.3 (2008): 519-533.
[9] P. Burkhart, T. Ely, C. Duncan, E. Lightsey, T. Campbell, A. Mogensen, Expected EDL navigation performance with spacecraft to spacecraft radiometric data, AIAA Guidance, Navigation, and Control Conference and Exhibit, 2005.
[10] T. Ely, D. Murphy, J. Seubert, J. Bell, D. Kuang, Expected performance of the deep space atomic clock mission, AAS/AIAA Space Flight Mechanics Meeting, 2014.
[11] E. Anzalone., C. Becker, D. Crump, D. Heater, Multi-spacecraft Autonomous Positioning System: LEO Demo Development, AIAA/USU Conference on Small Satellites, 2015.
[12] E. J. Anzalone, C. Becker, H. Sims, Initial Results of the Software-driven Navigation for Station Experiment, 2018 AIAA SPACE and Astronautics Forum and Exposition, 2018.
[13] https://www.nasa.gov/press-release/nasa-selects-experiments-for-possible-lunar-flights-in-2019
[14] J. Williams, Copernicus Version 4.6 Users Guide. NASA Johnson Space Center, April 2018.
[15] Small Spacecraft Systems Virtual Institute, State of the Art: Small Spacecraft Technology, NASA Ames Research Center. NASA/TP-2018-220027. https://sst-soa.arc.nasa.gov/download/1780/ , (accessed 03.06.2019).
[16] GPS Enhanced Onboard Navigation System, http://tco.gsfc.nasa.gov/downloads/featured_technologies/aerospace_aeronautics/geons_overview.pdf
[17] J. E. Donaldson, J. J. K. Parker, M. C. Moreau, D. E. Highsmith, and P. Martzen, Characterization of On-Orbit GPS Transmit Antenna Patterns for Space Users, Proceedings of the Institute of Navigation GNSS+, September 2018.